

Thorough numerical simulations of silicon heterojunction solar cells focusing on the sun-side-doped layer

Jiufang Han(韩久放), Yimeng Song(宋祎萌), Xiran Yu(于夕然), Conghui Jiang(姜聪慧), Wenxin Wang(王文新), Haiqiang Jia(贾海强), Chunhua Du(杜春花), and Hong Chen(陈弘)

Citation: Chin. Phys. B, 2025, 34 (**11**): 118801. DOI: 10.1088/1674-1056/addcc4
http://cpb.iphy.ac.cn; http://iopscience.iop.org/cpb

What follows is a list of articles you may be interested in

SolarDesign: An online photovoltaic device simulation and design platform

Wei E. I. Sha(沙威), Xiaoyu Wang(王啸宇), Wenchao Chen(陈文超), Yuhao Fu(付钰豪), Lijun Zhang(张立军), Liang Tian(田亮), Minshen Lin(林敏慎), Shudi Jiao(焦书迪), Ting Xu(徐婷), Tiange Sun(孙天歌), and Dongxue Liu(刘冬雪)

Chin. Phys. B, 2025, 34 (**1**): 018801. DOI: 10.1088/1674-1056/ad9017

Maskless fabrication of quasi-omnidirectional V-groove solar cells using an alkaline solution-based method

Xingqian Chen(陈兴谦), Yan Wang(王燕), Wei Chen(陈伟), Yaoping Liu(刘尧平), Guoguang Xing(邢国光), Bowen Feng(冯博文), Haozhen Li(李昊臻), Zongheng Sun(孙纵横), and Xiaolong Du(杜小龙)

Chin. Phys. B, 2024, 33 (**1**): 018801. DOI: 10.1088/1674-1056/ad0cd0

Micro-mechanism study of the effect of Cd-free buffer layers Zn*X*O (*X*=Mg/Sn) on the performance of flexible $Cu_2ZnSn(S, Se)^4$ solar cell

Caixia Zhang(张彩霞), Yaling Li(李雅玲), Beibei Lin(林蓓蓓), Jianlong Tang(唐建龙), Quanzhen Sun(孙全震), Weihao Xie(谢暐昊), Hui Deng(邓辉), Qiao Zheng(郑巧), and Shuying Cheng(程树英)

Chin. Phys. B, 2023, 32 (**2**): 028801. DOI: 10.1088/1674-1056/ac9b3a

Microstructure evolution and passivation quality of hydrogenated amorphous silicon oxide (a-SiO_x:H) on <100>- and <111>-orientated c-Si wafers

Jun-Fan Chen(陈俊帆), Sheng-Sheng Zhao(赵生盛), Ling-Ling Yan(延玲玲), Hui-Zhi Ren(任慧志), Can Han(韩灿), De-Kun Zhang(张德坤), Chang-Chun Wei(魏长春), Guang-Cai Wang(王广才), Guo-Fu Hou(侯国付), Ying Zhao(赵颖), Xiao-Dan Zhang(张晓丹)

Chin. Phys. B, 2020, 29 (**3**): 038801. DOI: 10.1088/1674-1056/ab6c47

Influence of interface states, conduction band offset, and front contact on the performance of a-SiC: H(n)/c-Si(p) heterojunction solar cells

Zhi Qiao(乔治), Jian-Li Ji(冀建利), Yan-Li Zhang(张彦立), Hu Liu(刘虎), Tong-Kai Li(李同锴)

Chin. Phys. B, 2017, 26 (**6**): 068802. DOI: 10.1088/1674-1056/26/6/068802

Thorough numerical simulations of silicon heterojunction solar cells focusing on the sun-side-doped layer

Jiufang Han(韩久放)[1,2,3,†], Yimeng Song(宋祎萌)[4,†], Xiran Yu(于夕然)[1,2,3], Conghui Jiang(姜聪慧)[5], Wenxin Wang(王文新)[1,6], Haiqiang Jia(贾海强)[1,2,3,7], Chunhua Du(杜春花)[1,3,6,‡], and Hong Chen(陈弘)[1,2,3,6,7,§]

[1] *Key Laboratory for Renewable Energy, Beijing Key Laboratory for New Energy Materials and Devices, Beijing National Laboratory for Condensed Matter Physics, Institute of Physics, Chinese Academy of Sciences, Beijing* 100190, *China*
[2] *Second Affiliation University of Chinese Academy of Sciences, Beijing* 100049, *China*
[3] *Third Affiliation School of Physical Sciences, University of Chinese Academy of Sciences, Beijing* 100049, *China*
[4] *Guangdong Provincial Key Laboratory of Electronic Functional Materials and Devices, Huizhou University, Huizhou* 516000, *China*
[5] *Jiangsu Key Laboratory of Advanced Negative Carbon Technologies, Institute of Functional Nano & Soft Materials (FUNSOM), Soochow University, Suzhou* 215123, *China*
[6] *The Yangtze River Delta Physics Research Center, Liyang* 213000, *China*
[7] *Songshan Lake Materials Laboratory, Dongguan* 523808, *China*

(Received 22 April 2025; revised manuscript received 22 April 2025; accepted manuscript online 23 May 2025)

To improve the photovoltaic conversion efficiency (PCE) of silicon heterojunction (SHJ) solar cells, this study focuses on optimizing the physical parameters of the sun-side-doped layer and proposes strategies to address the challenges posed by Fermi level pinning in wide bandgap designs. Using AFORS-HET simulations, we systematically investigate the effects of bandgap width, doping concentration, and defect state distribution on the energy band structure, interface electric field, and carrier transport dynamics. The results reveal that maintaining the Fermi level within 0.3 eV of the conduction band is essential for optimal device performance. A wider bandgap (> 1.8 eV) enhances the utilization of short-wavelength light and significantly suppresses interface recombination, leading to an increase in short-circuit current density (J_{sc}) by 0.8 mA/cm^2. This benefit comes with a delicate balance between minimizing defect state density and improving doping efficiency. This study provides theoretical insights into the optimization of doped layer physical parameters and proposes practical solutions, including nano-crystallization and low-doping interface strategies, to improve the performance of SHJ solar cells and support industrial applications.

Keywords: silicon heterojunction (SHJ) solar cell, AFORS-HET, numerical simulation, Fermi level pinning

PACS: 88.40.hj, 52.50.–b, 61.72.uf

DOI: 10.1088/1674-1056/addcc4 **CSTR:** 32038.14.CPB.addcc4

1. Introduction

Silicon heterojunction (SHJ) solar cells have emerged as leading candidates for high-efficiency photovoltaic devices due to their superior photoelectric conversion efficiency (PCE) and potential for cost-effective manufacturing.[1–3] As commercialization advances, SHJ solar cells consistently set new PCE records.[4] However, the actual efficiency still falls short of the theoretical limit of 28.5% for SHJ solar cells.[5–7]

Addressing this challenge requires continuous advancements in materials and device designs, particularly in optimizing the doped layers on the sun side, which play a critical role in light absorption, carrier transport, and interface recombination control.[3,8,9] An optimal-doped layer should: (i) have a low optical absorption coefficient to minimize parasitic absorption; (ii) exhibit low activation energy and defect density to reduce recombination and enhance carrier transport; (iii) feature a band offset that facilitates selective carrier extraction. Extensive studies have explored the use of alternative materials to hydrogenated amorphous silicon (a-Si:H), including hydrogenated amorphous silicon carbide (a-SiC$_x$:H) and hydrogenated amorphous silicon oxide (a-SiO$_x$:H), to mitigate parasitic absorption and enhance carrier collection.[10–12] Incorporating nanocrystals further reduces the absorption coefficient while enhancing doping efficiency and conductivity.[12,13] Replacing a-Si:H with a-SiO$_x$:H films reduces short-wavelength absorption coefficients, increasing short-circuit current density (J_{sc}) by 0.13 mA/cm^2.[14] A dual-layer doped structure based on p-nc-SiO$_x$:H and p-nc-Si:H facilitates efficient hole collection, achieving an SHJ solar cells with a fill factor (FF) ranging from 83%–86%.[15] Using p-nc-Si:H thin layers grown by VHF-PECVD as the sun-side-doped layer increases J_{sc} due to reduced parasitic absorption, while improving open-circuit voltage (V_{oc}) and FF due to better passivation and electrical contact, leading to a PCE improvement of 7.2%.[16] Addition-

[†]These authors contributed equally to this work.
[‡]Corresponding author. E-mail: duchunhua@iphy.ac.cn
[§]Corresponding author. E-mail: hchen@iphy.ac.cn

© 2025 Chinese Physical Society and IOP Publishing Ltd. All rights, including for text and data mining, AI training, and similar technologies, are reserved.

ally, employing n-nc-SiO$_x$:H as the front-doped layer minimizes parasitic absorption, resulting in a PCE of 26.74% and a J_{sc} of 41.16 mA/cm^2.[17]

Optimizing doped layer materials requires a balanced consideration of multiple physical properties. For instance, reducing optical absorption to suppress parasitic losses often demands widening the bandgap, while enhancing conductivity may involve introducing nanocrystallinity. These strategies, however, can simultaneously alter the electronic band structure of the doped layer, including not only the bandgap width but also the absolute positions of the valence and conduction bands. Such changes inevitably affect the band alignment at the SHJ device interface and influence carrier transport dynamics.[18,19] Therefore, precise control over the physical parameters of the doped layer is essential to ensure optimal device performance, and the need for a systematic investigation into the physical properties of doped layers is highlighted.

This work focuses on addressing the limitations imposed by Fermi-level pinning in wide-bandgap-doped layers, which restrict their practical application despite their theoretical advantages. To overcome the high costs associated with experimental iterations, we employ AFORS-HET software to simulate SHJ solar cells.[20–22] This software facilitates precise parameter optimization and comprehensive evaluation of strategies for enhancing PCE.[23–25] We systematically investigate the effects of bandgap width, doping concentrations, and defect state distributions on the energy band structure, carrier transport, and recombination dynamics. Our results highlight the potential of wide-bandgap-doped layers to reduce parasitic absorption and enhance carrier extraction efficiency. Furthermore, we propose physical optimization strategies, including defect state management and doping control, to mitigate Fermi-level pinning. We also introduce design principles involving nano-crystallization and buffer-layer approaches to minimize recombination losses and improve PCE. These findings offer a new perspective on doped-layer engineering and provide practical guidelines for optimizing SHJ solar cell performance.

2. Methods

A set of a-Si:H and a-SiC$_x$:H films were prepared using silane (SiH$_4$), methane (CH$_4$), and hydrogen (H$_2$) gases in a capacitively-coupled PECVD (13.56 MHz) system, maintaining a working pressure of 120 Pa. The films were grown on glass substrates, using applied RF power of 25 mW·cm^{-2}, at a low growth temperature of $\sim$ 200 °C. The samples were grown with the varying H$_2$-dilution ratio $R(\mathrm{H_2}) = [\mathrm{H_2}]/[\mathrm{SiH_4}+\mathrm{CH_4}]$ from 5 to 120 and CH$_4$ ratio $R(\mathrm{CH_4}) = [\mathrm{CH_4}]/[\mathrm{SiH_4}]$ from 0 to 2. The initial base vacuum in the PECVD reactor before plasma ignition was retained at $\sim 10^{-5}$ Pa. The typical thickness of the samples deposited on the glass substrates was maintained at 40 nm–200 nm. If a post-annealing process is mentioned, the annealing is carried out in a nitrogen atmosphere at a temperature of 300 °C for 2 hours. The optical transmission data were recorded using a Shimadzu UV-3600i Plus, UV-VIS-NIR spectrophotometer. The crystallinity of the grown film network was estimated using a Raman spectrometer (Jobin Yvon JY-T64000) with a 532-nm laser at a low power density of $\sim$ 2 mW·cm^{-2}.

When performing simulations of SHJ solar cells, the distribution of carriers and electric fields inside the solar cell is obtained by solving a set of partial differential equations, including the one-dimensional (1D) Poisson's equation and the continuity equations.

The 1D Poisson's equation, which is to be solved at each x, reads

$$\frac{\varepsilon_r\varepsilon_0(x)}{q}\frac{\partial^2\varphi(x,t)}{\partial x^2} = p(x,t) - n(x,t) + N_D(x) - N_A(x) + \rho_{trap}(x,t), \quad (1)$$

where ε_r and ε_0 are the relative and vacuum dielectric constants, q is the electron charge, p and n are the hole and electron densities, N_D and N_A are the donor and acceptor doping concentrations, and ρ_{trap} is the total charge trapped by defects. And the 1D continuity equations are

$$-\frac{1}{q}\frac{\partial j_n(x,t)}{\partial x} = G_n(x,t) - R_n(x,t) - \frac{\partial}{\partial t}n(x,t), \quad (2a)$$

$$+\frac{1}{q}\frac{\partial j_p(x,t)}{\partial x} = G_p(x,t) - R_p(x,t) - \frac{\partial}{\partial t}p(x,t), \quad (2b)$$

where G is the carrier generation rate, R is the carrier recombination rate, and j is the current density.

To investigate the impact of physics parameters of the sun-side-doped layer on SHJ solar cell performance, an n-SiC$_x$:H layer will be introduced into the simulated structure as the doped layer on the sun side, as the basis of all the parameter changes. Additionally, the insertion of a hydrogenated intrinsic amorphous silicon (i-a-Si:H) layer between the p-c-Si wafer and doped layer (n-SiC$_x$:H or p-a-Si:H) was considered. The focus of our investigation was on the band gap width, defect state distribution, and doping level of the n-SiC$_x$:H layer. Figure 1(a) is a schematic diagram of the simulated SHJ solar cell structure. The SHJ solar cells were simulated based on p-doped monocrystalline Si wafers (150 μm).

In the simulation, AM 1.5 radiation was used as the illumination source with a power density of 100 mW·cm^{-2}. The main simulated parameters of the different layers are listed in Table 1.[26,27] The main defects of a-Si:H and n-SiC$_x$:H deposited by PECVD include band tail states caused by periodic damage and dangling bonds incompletely passivated by hydrogen atoms, which were characterized by the Urbach tail and Gaussian models, as shown in Fig. 1(b). It was assumed that the position of the characteristic energy of the Gaussian defect state in the band gap is linearly related to the width of

the band gap. The position of characteristic energy (calculated from the characteristic energy to the conduction band bottom), along with the specific values of the total density of different defect states are provided in Table 2. Meanwhile, the band tail states are set to fixed values.

For the p-c-Si substrate, oxygen defects with a density of 1×10^{10} cm^{-3}·eV^{-1}, located at 0.56 eV above the valance band top, were assumed. A flat band was applied to the front and back contacts to negate any contact potential. The surface recombination velocity of both electrons and holes was set at 1×10^{7} cm·s^{-1}. During the simulation process, all these parameters were taken into account except for instances where specific variables were to be considered.

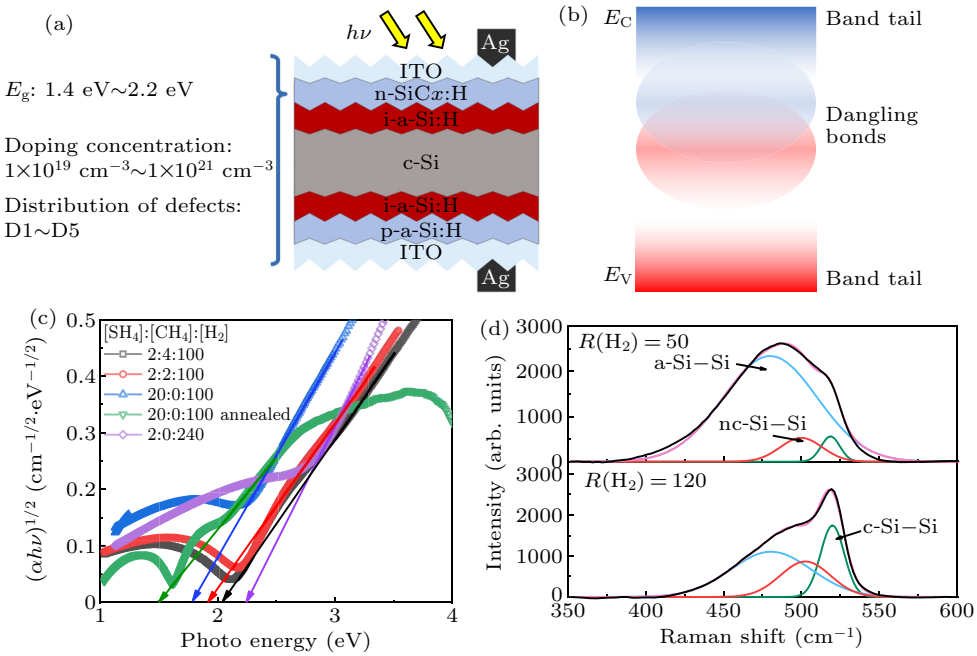


Fig. 1. (a) Cross-sectional schematic diagram of an SHJ solar cell, illustrating the main variables used in the simulations. (b) Schematic depiction of the defect distribution within the n-SiC$_x$:H layer on the sun side of the SHJ solar cell. (c) UV-VIS-NIR transmittance data and (d) Raman spectra of PECVD-deposited films under varying gas flow rates.

Table 1. The main input parameter values for AFORS-HET simulation.

Parameters	c-p-Si	i-a-Si:H	p-a-Si:H	n-SiC$_x$:H
Layer thickness (nm)	1.5×10^{5}	10	10	10
Dielectric constant	11.9	11.9	11.9	11.9
Electron affinity (eV)	4.05	3.8	3.85	3.85
Band gap (eV)	1.12	1.72	1.74	1.4∼2.2
Effective conduction band density (cm^{-3})	2.8×10^{19}	1×10^{20}	1×10^{20}	1×10^{20}
Effective valence band density (cm^{-3})	1.04×10^{19}	1×10^{20}	1×10^{20}	1×10^{20}
Electron mobility (cm^2·V^{-1}·s^{-1})	1041	20	20	20
Hole mobility (cm^2·V^{-1}·s^{-1})	418	5	5	5
Acceptor concentration (cm^{-3})	2×10^{17}	0	1×10^{20}	0
Donor concentration (cm^{-3})	0	0	0	$1 \times 10^{19} \sim 1 \times 10^{21}$
Layer density (g·cm^{-3})	2.328	2.328	2.328	2.328
Thermal velocity of electrons (cm·s^{-1})	1×10^{7}	1×10^{7}	1×10^{7}	1×10^{7}
Thermal velocity of holes (cm·s^{-1})	1×10^{7}	1×10^{7}	1×10^{7}	1×10^{7}
Auger recombination coefficient for electron (hole) (cm^6·s^{-1})	2.2×10^{-31} (9.9×10^{-32})	0 (0)	0 (0)	0 (0)
Direct band-to-band recombination coefficient (cm^3·s^{-1})	0	0	0	0

Table 2. The main input of defect state distributions of n-SiC$_x$:H layer.

Band gap (eV)	1.4	1.6	1.8	2.0	2.2
Characteristic energy of dangling bonds (doner) (eV)	0.41	0.47	0.52	0.58	0.64
Characteristic energy of dangling bonds (acceptor) (eV)	0.49	0.56	0.63	0.70	0.77
Defect state distribution	D1	D2	D3	D4	D5
The total defect density of dangling bonds (cm^{-3})	1×10^{19}	5×10^{19}	1×10^{20}	5×10^{20}	1×10^{21}
Sigma (eV)	0.21	0.21	0.21	0.21	0.21
The total density of band tail state (cm^{-3})	1×10^{20}	1×10^{20}	1×10^{20}	1×10^{20}	1×10^{20}
Urbach energy (eV)	0.068	0.068	0.068	0.068	0.068

3. Results

We used the UV-VIS-NIR transmittance data of the prepared a-SiC$_x$:H, a-Si:H, and μc-Si:H thin films to investigate their optical properties across a range of gas flow ratios, which are detailed in Fig. 1(c). Tauc's relation was employed to estimate the optical bandgap of the films, and the Urbach energy can also be obtained by fitting the optical absorption spectrum.[28] Figure 1(c) shows that as the $R(CH_4)$ increases from 0 to 2, the optical bandgap of the films rises from 1.78 eV to 2.05 eV. When $R(H_2)$ reaches 120, the optical bandgap dramatically increases to 2.25 eV, without the presence of CH_4 gas. In films that underwent low-temperature annealing after deposition, the optical bandgap decreases to 1.50 eV, with the lower inverse slope reflecting an increase in disorder due to the removal of H atoms.[29] The corresponding Urbach energy increases with increasing $R(CH_4)$, decreases with increasing $R(H_2)$, and also decreases after annealing, ranging from 63 meV to 342 meV.

Figure 1(d) presents the Raman spectra of the Si–Si bonding band in μc-Si:H films prepared at different H_2 dilution ratios, $R(H_2) = 50$ and 120. The main peak are at ~ 480 cm^{-1} for the a-Si–Si component, ~ 501 cm^{-1} for the nc-Si–Si component, and at ~ 520 cm^{-1} for the c-Si–Si component.[28] As $R(H_2)$ increases, the relative area ratio of the a-Si–Si component peak decreases, while the crystalline component grows. The crystallization rate is calculated based on the ratio of the crystalline component peak area to the total peak area. Across the range of $R(H_2)$ from 5 to 120, the crystallization rate varies from 0 to 76.20%. The physical parameters measured from all the films provide a basis for numerical simulations described later.

We conducted numerical simulations to investigate how variations in bandgap width, doping concentration, and defect state distribution influence the Fermi-level position and overall device performance. Figure 2 illustrates the simulation results based on two defect density groups, D1 and D3, with doping concentrations ranging from 1×10^{19} cm^{-3} to 1×10^{21} cm^{-3}.

For low-defect density layers (D1 group), devices with doping concentrations below 5×10^{19} cm^{-3} exhibited a sharp drop in both V_{oc} and FF as the bandgap widened from 1.4 eV to 2.2 eV. This parameter region is referred to as a dead zone in this article, as indicated by the dashed box in Fig. 2. While, higher doping levels ($> 5 \times 10^{19}$ cm^{-3}) successfully suppressed the dead zone, enabling stable performance even at wider bandgaps.

Compared with the D1 group, the simulation results of the high-defect density group (D3) exhibit a similar variation trend, as shown in Fig. 2(b). However, the doping level required for SHJ solar cells to avoid the dead zone significantly is significantly higher in the D3 group. With increasing bandgap width, this required doping level continues to rise. Specifically, unlike the D1 group, where lower doping concentrations maintain stable performance, the D3 group requires a doping concentration of 1×10^{20} cm^{-3} to sustain normal efficiency at bandgaps of 1.4 eV and 1.6 eV. Beyond this range, as the bandgap increases, the overall efficiency sharply decline, leading to the formation of a dead zone. The formation of the dead zone and its deep relationship with the position of the Fermi level will be further discussed later.

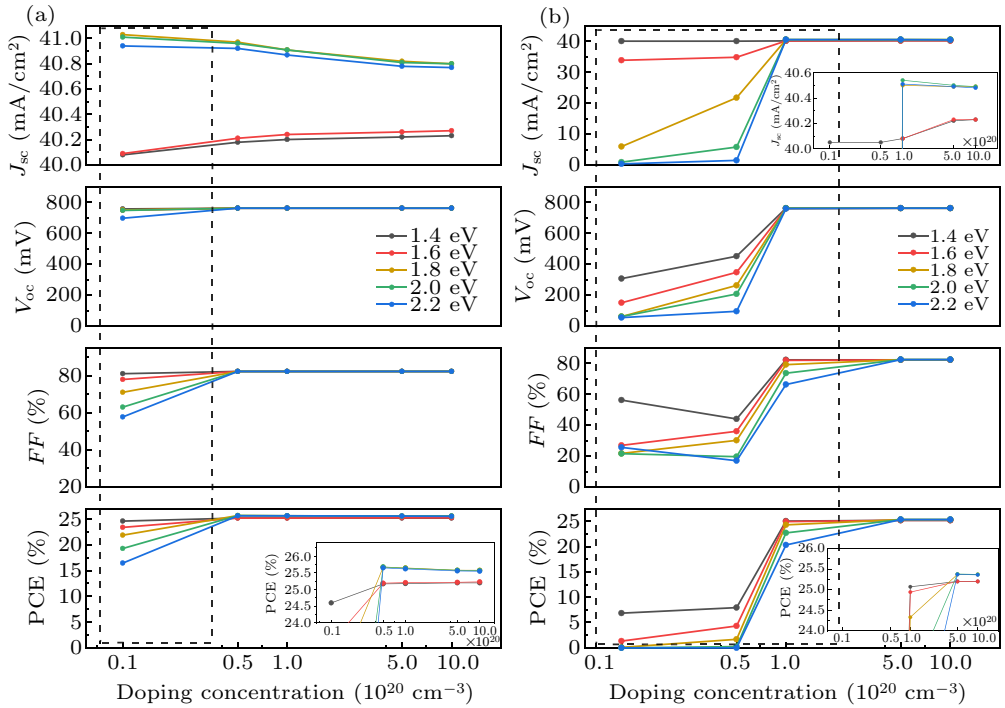


Fig. 2. Simulation results of SHJ solar cells with varying bandgap widths and doping levels, corresponding to defect distributions of (a) D1 and (b) D3.

Furthermore, when the doping concentration exceeds a certain threshold, above 5×10^{19} cm^{-3} for the D1 group and above 5×10^{20} cm^{-3} for the D3 group, the efficiency curves of the solar cells split into two distinct groups, with efficiencies of 25.0% and 25.5%, respectively. This divergence is more pronounced in the magnified images embedded in Figs. 2(a) and 2(b), which is mainly attributed to the difference in J_{sc}. Similar trends can be observed in the magnified J_{sc} curves for the D1 and D3 groups. To further investigate these phenomena and provide practical guidance for optimizing solar cell design and fabrication, a more detailed analysis is presented in the subsequent sections.

4. Discussion

To investigate the origin of the dead zone, we performed detailed simulations focused on the boundary region of the D3 group, specifically SHJ solar cells with a doping concentration of 1×10^{20} cm^{-3}. Figure 3(a) displays the *I*–*V* and *P*–*V* curves under illumination, with *P*–*V* curves shown in lighter shades for clarity. As the bandgap widens, the J_{sc} in the *I*–*V* curves exhibits a slight increase. However, a gradual transition from a standard *I*–*V* shape to an S-shaped curve is observed. This S-shaped distortion shifts the power peak leftward in the *P*–*V* curves, reducing the *FF* from 82.1% at 1.4 eV to 65.6% at 2.2 eV. Previous studies attribute this phenomenon to band mismatches at the heterojunction interface.[30]

Figure 3(b) further illustrates the distribution of n-type carriers within the doped layer as a function of bandgap width. A larger bandgap reduces the carrier concentration, impairing transport efficiency and lowering overall device performance.

Variations in bandgap width, doping levels, and defect distributions directly influence the Fermi level position, as shown in the heatmap in Fig. 3(c). The energy difference (δE) between the Fermi level and the conduction band edge decreases as the color transitions from red to blue. In Fig. 3(c), the dashed region highlights the parameter range associated with the dead zone observed in Fig. 2(b). Devices enter the dead zone when δE exceeds 0.3 eV, whereas maintaining δE below this threshold (blue regions) prevents performance degradation. This highlights the strong correlation between Fermi-level position and the performance of the SHJ device.

As the bandgap widens, the likelihood of Fermi-level pinning increases due to the displacement of dangling bond energy levels further from the conduction band. This necessitates higher doping concentrations to compensate for defect states, creating a delicate tradeoff between minimizing defect density and enhancing doping efficiency.

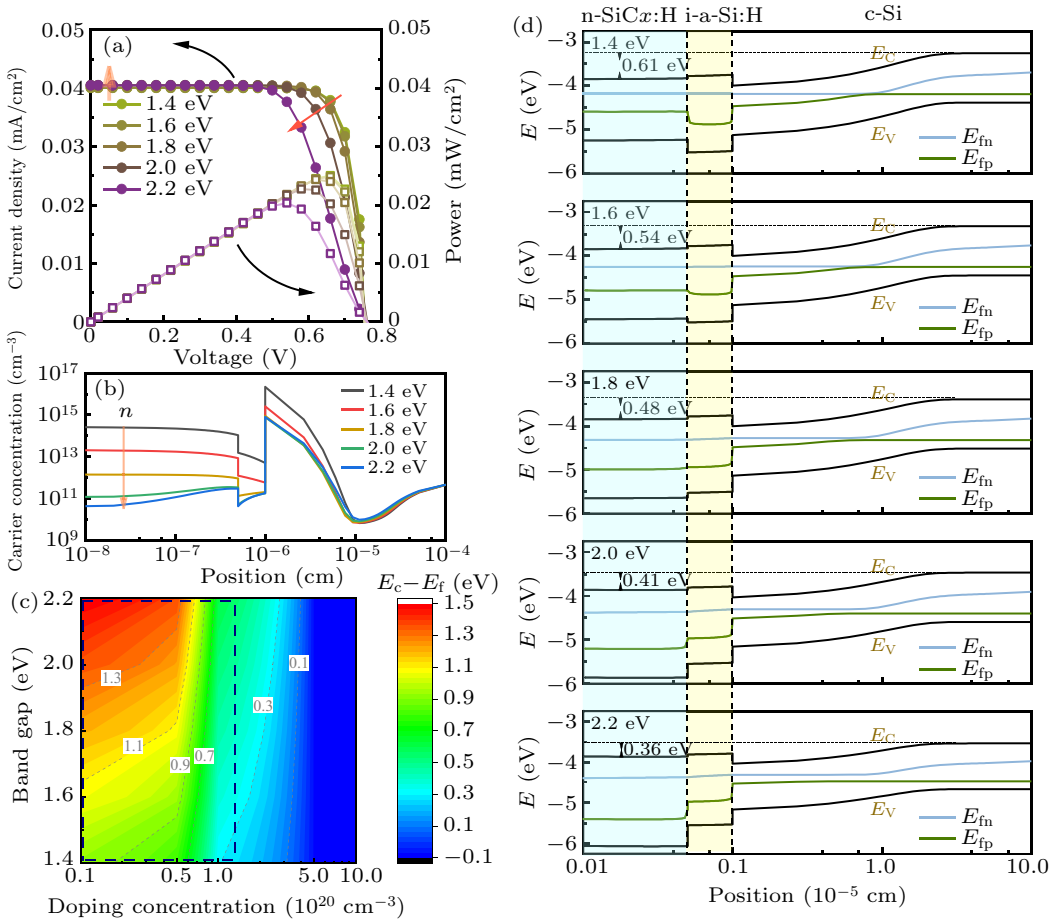


Fig. 3. (a) The *I*–*V* and *P*–*V* curves, and (b) the distribution of n-type charge carriers in SHJ solar cells simulated with varying bandgap widths, corresponding to the defect distribution of D3 and a doping concentration of 1×10^{20} cm^{-3}, respectively. (c) Heatmap of the Fermi level position corresponding to the same defect distribution (D3). (d) Energy band diagrams under identical conditions.

Figure 3(d) presents the corresponding band diagrams for varying bandgap widths. The conduction band offset (marked by double arrows) decreases as the bandgap widens, contributing to the development of the S-shaped *I*–*V* curves and further reductions in *FF*.[31]

While widening the bandgap reduces parasitic absorption and optical losses, it introduces structural challenges that require careful consideration. Specifically, higher doping concentrations may increase defect densities, leading to stronger Fermi-level pinning and performance degradation.

Although the simulated doping concentrations range from 1×10^{19} cm^{-3} to 1×10^{21} cm^{-3}, we emphasize that this analysis serves as a qualitative investigation to capture general trends in electrical behavior. In deposition processes, the total number of dopant atoms introduced into the film can indeed reach the 10^{21} cm^{-3} level. However, in amorphous and nanocrystalline silicon, the effective doping efficiency is typically limited due to compensation by defect states, resulting in the Fermi level remaining not less than 0.1 eV away from the conduction or valence band edges. Nevertheless, recent studies have demonstrated that post-deposition treatments such as light soaking can significantly enhance dopant activation and improve effective doping in hydrogenated amorphous silicon, suggesting potential pathways to overcome this limitation in practical applications.[32] In practical scenarios, figure 4(a) shows that defect state densities scale linearly with doping concentrations, ranging from D1 to D5. As depicted in Fig. 4(b), this correlation amplifies Fermi-level pinning effects, particularly in wide-bandgap configurations. Therefore, optimizing doping profiles and minimizing defect densities through nano-crystallization techniques is essential for maintaining electrical performance.

To further investigate the underlying mechanisms responsible for the bifurcation of solar cell efficiency curves into high- and low-performance categories as the bandgap width varies, we performed detailed simulations. We simulated the external quantum efficiency (EQE) curves, shown in Fig. 5(a), which revealed a distinct segmentation in EQE behavior as the bandgap width varied. Notably, SHJ solar cells with larger bandgaps exhibited higher EQE values, especially in the short-wavelength region.

We also simulated the evolving trends of J_{sc} and PCE under different bandgap widths while maintaining the defect state distribution of D1 and a doping concentration of 1×10^{20} cm^{-3}, as shown in Fig. 5(b). A sharp performance transition was observed around a bandgap width of 1.7 eV.

The differences in EQE at short wavelengths primarily result from variations in parasitic absorption and carrier transport dynamics in the light-receiving regions. Figure 5(c) illustrates the corresponding band diagrams of the sun side under different bandgap conditions. As the bandgap of the doped layer increases, the relative alignment between the valence band of the doped layer and the intrinsic layer shifts. Specifically, at 1.4 eV and 1.6 eV, the valence band of the doped layer lies above that of the intrinsic passivation layer. However, when the bandgap widens to 1.8 eV, the positions are reversed. Simultaneously, the quasi-Fermi level gradient for holes at the interface is inverted, which facilitates the extraction of photogenerated carriers from the illuminated surface region (including the doped and passivation layers). This trend is consistent with the EQE results shown in Fig. 5(a). Notably, a sharp improvement in J_{sc} is observed when the bandgap reaches around 1.7 eV, which corresponds to a critical transition point in the interface band alignment. This transition enhances carrier selectivity and extraction efficiency, especially in the front-side layers, contributing to the observed performance jump.

Figures 5(d) and 5(e) illustrate the simulated carrier distributions and recombination rates for bandgap widths of 1.6 eV and 2.0 eV, respectively. In structures with narrower bandgaps, insufficient band offsets lead to potential barriers that trap minority carriers at the interface, causing elevated recombination rates. In contrast, wider bandgaps reduce carrier recombination, resulting in more efficient carrier extraction.

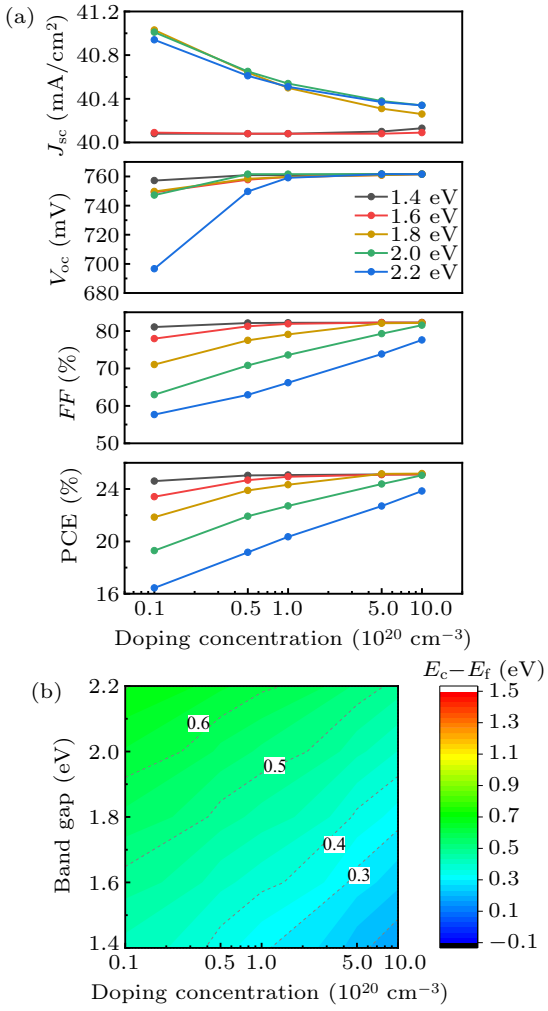


Fig. 4. (a) Simulation results of SHJ solar cells, and (b) heatmap of the Fermi level position, where the defect distribution in the n-SiC$_x$:H layer is linearly correlated with the doping concentration.

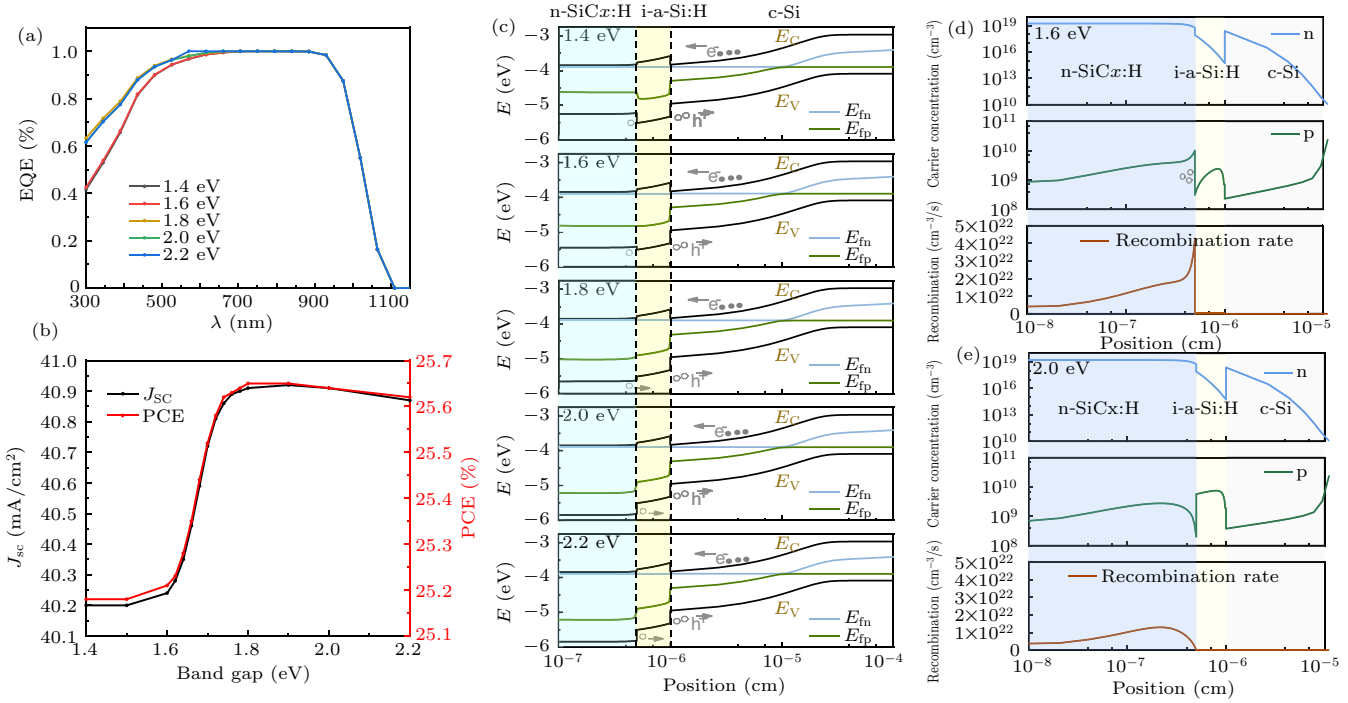


Fig. 5. (a) External quantum efficiency graph, (b) J_{sc} and PCE trends, and (c) energy band diagram of SHJ solar cells with varying bandgap widths, corresponding to the defect distribution of D1 and a doping concentration of 1×10^{20} cm^{-3}, respectively. Carrier distribution and recombination rates under the same conditions are simulated for bandgap widths of (d) 1.6 eV and (e) 2.0 eV.

These simulations highlight that wider bandgap-doped layers significantly enhance carrier extraction and separation on the sun side, particularly for short-wavelength light. The improved transport dynamics and reduced recombination losses, observed through EQE and recombination rate analyses, underscore the potential of wide-bandgap materials to optimize SHJ solar cell performance. However, it should be noted that the AFORS-HET simulation tool used in this study does not explicitly account for tunneling effects, particularly those assisted by band tail states. This limitation may lead to discrepancies between simulation and real device performance, especially under strong interfacial electric fields or large band offsets where tunneling plays a non-negligible role.

As discussed earlier, incorporating a wider bandgap in the sun-side-doped layer significantly enhances carrier transport and separation at the front surface, thereby improving the overall photoelectric conversion efficiency of SHJ photovoltaic devices. However, the use of wide-bandgap materials also increases the likelihood of Fermi-level pinning, particularly when compared to traditional a-Si:H doped layers. This effect can degrade device performance, emphasizing the need for careful material and process optimization.

Simulations reveal that achieving optimal performance with wide-bandgap doped layers requires a delicate balance between minimizing defect state density and optimizing doping efficiency. Specifically, Fermi-level pinning becomes more pronounced as the bandgap widens, necessitating higher doping concentrations to compensate for defect states and avoid performance degradation. At the same time, excessive defect densities amplify recombination losses, especially at the interface between the wide-bandgap doped layer and the a-Si:H passivation layer. Despite these challenges, wider bandgaps effectively reduce parasitic absorption and improve short-wavelength utilization, provided that a stable band alignment and low recombination rates can be maintained.

To address these challenges, several optimization strategies can be employed. Nano-crystallization has proven to be an effective approach, as it reduces the density of dangling bonds, enhances doping efficiency, and improves doping levels at the same concentration. Additionally, interface engineering is critical for mitigating recombination losses caused by band offsets at the interface between the doped layer and the passivation layer. As shown in Fig. 5, reducing the doping concentration at this interface, or introducing a thin intrinsic wide-bandgap buffer layer, can smooth transitions and suppress recombination. Furthermore, strict quality control is essential for wide-bandgap doped layers, as their photosensitivity serves as a key metric for evaluating material performance. These insights highlight the importance of carefully engineered materials and deposition processes to balance bandgap widening and carrier transport efficiency.

The findings above provide clear design principles and process guidelines for optimizing wide-bandgap doped layers in SHJ solar cells. These strategies, derived from systematic simulations, are relatively straightforward to implement in large-scale industrial production. By reducing costs and improving efficiency, these methods are expected to accelerate the commercialization of SHJ photovoltaic technologies.

5. Conclusion and perspectives

The results demonstrate that wider bandgap doped layers in SHJ solar cells effectively optimize carrier extraction on the sun side while reducing parasitic absorption. Simulation data indicate that these layers are more susceptible to Fermi level pinning caused by excessive defect states. When the Fermi level is maintained within 0.3 eV of the conduction band, the adverse effects of Fermi level pinning on device performance is significantly reduced. Consequently, the critical role of nano-crystallization in enhancing the applicability of wide-bandgap-doped layers is highlighted. Additionally, the introduction of lower doping levels or intrinsic transition layers within wide-bandgap-doped layers is proposed as a viable strategy to optimize carrier extraction and concurrently suppress carrier recombination.

Acknowledgements

Project supported by the National Natural Science Foundation of China (Grant Nos. 61991441 and 62004218), the Strategic Priority Research Program of the Chinese Academy of Sciences (Grant No. XDB01000000), and the Youth Innovation Promotion Association of the Chinese Academy of Sciences (Grant No. 2021005).

References

[1] De Wolf S, Descoeudres A, Holman Z C and Ballif C 2012 *Green* **2** 7
[2] Razzaq A, Allen T G, Liu W, Liu Z and De Wolf S 2022 *Joule* **6** 514
[3] Jiang C, Zhang G, Hong Z, Chen J, Li Y, Yuan X, Lin Y, Yu C, Wang T and Song T 2023 *Adv. Mater.* **35** 2208042
[4] Duan W, Lambertz A, Bittkau K, Qiu D, Qiu K, Rau U and Ding K 2021 *Progress in Photovoltaics: Research and Applications* **30** 384
[5] Yoshikawa K, Kawasaki H, Yoshida W, Irie T, Konishi K, Nakano K, Uto T, Adachi D, Kanematsu M, Uzu H and Yamamoto K 2017 *Nature Energy* **2** 17032
[6] Kerr M J, Cuevas A and Campbell P 2003 *Progress in Photovoltaics: Research and Applications* **11** 97
[7] Long W, Yin S, Peng F, Yang M, Fang L, Ru X, Qu M, Lin H and Xu X 2021 *Sol. Energy Mater. Sol. Cells* **231** 111291
[8] Huang S, Xu C, Wang G, Du J, Yu J, Zhang L, Meng F, Zhao D, Li R, Huang H, Liu Z and Liu W 2024 *Mater. Lett.* **357** 135768
[9] Hao B, Song Y, Jiang C, Han J, Jiang Y, Deng Z, Wang W, Jia H, Chen H and Du C 2023 *JaJAP* **62** 061002
[10] Boccard M and Holman Z C 2015 *JAP* **118** 065704
[11] Köhler M, Pomaska M, Procel P, Santbergen R, Zamchiy A, Macco B, Lambertz A, Duan W, Cao P, Klingebiel B, Li S, Eberst A, Luysberg M, Qiu K, Isabella O, Finger F, Kirchartz T, Rau U and Ding K 2021 *Nature Energy* **6** 529
[12] Pomaska M, Köhler F, Zastrow U, Mock J, Pennartz F, Muthmann S, Astakhov O, Carius R, Finger F and Ding K 2016 *JAP* **119** 175303
[13] Mandal S, Das G, Dhar S, Tomy R M, Mukhopadhyay S, Banerjee C and Barua A K 2015 *MCP* **157** 130
[14] Jiang K, Liu W, Yang Y, Yan Z, Huang S, Li Z, Li X, Zhang L and Liu Z 2021 *Journal of Materials Science: Materials in Electronics* **33** 416
[15] Zhao Y, Procel P, Han C, Mazzarella L, Yang G, Weeber A, Zeman M and Isabella O 2021 *Sol. Energy Mater. Sol. Cells* **219** 110779
[16] Umishio H, Sai H, Koida T and Matsui T 2020 *Progress in Photovoltaics: Research and Applications* **29** 344
[17] Lin H, Yang M, Ru X, Wang G, Yin S, Peng F, Hong C, Qu M, Lu J, Fang L, Han C, Procel P, Isabella O, Gao P, Li Z and Xu X 2023 *Nature Energy* **8** 789
[18] Liu W, Zhang L, Yang X, Shi J, Yan L, Xu L, Wu Z, Chen R, Peng J, Kang J, Wang K, Meng F, De Wolf S and Liu Z 2020 *Joule* **4** 913
[19] Khokhar M Q, Mallem K, Fan X, Kim Y, Hussain S Q, Cho E C and Yi J 2022 *ECS Journal of Solid State Science and Technology* **11** 085001
[20] Varache R, Leendertz C, Gueunier-Farret M E, Haschke J, Muñoz D and Korte L 2015 *Sol. Energy Mater. Sol. Cells* **141** 14
[21] Mazzarella L, Morales-Vilches A B, Hendrichs M, Kirner S, Korte L, Schlatmann R and Stannowski B 2017 *IEEE Journal of Photovoltaics* **8** 70
[22] Qiu D, Duan W, Lambertz A, Bittkau K, Steuter P, Liu Y, Gad A, Pomaska M, Rau U and Ding K 2020 *Sol. Energy Mater. Sol. Cells* **209** 110471
[23] Alkharasani W M, Amin N, Shahahmadi S A, Alkahtani A A, Mohamad I S B, Chelvanathan P and Sieh Kiong T 2022 *Materials* **15** 3508
[24] Deka H, Sunaniya A and Agarwal P 2022 *IEEE Journal of Photovoltaics* **12** 204
[25] Kanneboina V 2020 *Journal of Computational Electronics* **20** 344
[26] Riaz M, Kadhim A C, Earles S K and Azzahrani A 2018 *Opt. Express* **26** A626
[27] Zhao L, Wang G, Diao H and Wang W 2018 *J. Phys. D: Appl. Phys.* **51** 045501
[28] Dey A and Das D 2022 *ApSS* **597** 153657
[29] Berntsen A J, van der Weg W F, Stolk P A and Saris F W 1993 *Phys. Rev. B* **48** 14656
[30] Saive R 2019 *IEEE Journal of Photovoltaics* **9** 1477
[31] Obikoya G D, Soman A, Das U K and Hegedus S S 2023 *Sol. Energy Mater. Sol. Cells* **263** 112586
[32] Liu W, Shi J, Zhang L, Han A, Huang S, Li X, Peng J, Yang Y, Gao Y and Yu J 2022 *Nature Energy* **7** 427